Official journal of the CIOMP 2047-7538
www.nature.com/lsa

ARTICLE Open Access

Shipborne oceanic high-spectral-resolution lidar for accurate estimation of seawater depth-resolved optical properties

Yudi Zhou[1,2], Yang Chen[1], Hongkai Zhao[1], Cédric Jamet[3], Davide Dionisi[4], Malik Chami[5], Paolo Di Girolamo[6], James H. Churnside[7], Aleksey Malinka[8], Huade Zhao[9], Dajun Qiu[10], Tingwei Cui[11], Qun Liu[1], Yatong Chen[1], Sornsiri Phongphattarawat[12], Nanchao Wang[1], Sijie Chen[1], Peng Chen[13], Ziwei Yao[9], Chengfeng Le[14], Yuting Tao[1], Peituo Xu[1], Xiaobin Wang[1], Binyu Wang[1], Feitong Chen[1], Chuang Ye[1], Kai Zhang[1], Chong Liu[1] and Dong Liu[1,2,15]✉

Abstract

Lidar techniques present a distinctive ability to resolve vertical structure of optical properties within the upper water column at both day- and night-time. However, accuracy challenges remain for existing lidar instruments due to the ill-posed nature of elastic backscatter lidar retrievals and multiple scattering. Here we demonstrate the high performance of, to the best of our knowledge, the first shipborne oceanic high-spectral-resolution lidar (HSRL) and illustrate a multiple scattering correction algorithm to rigorously address the above challenges in estimating the depth-resolved diffuse attenuation coefficient K_d and the particulate backscattering coefficient b_{bp} at 532 nm. HSRL data were collected during day- and night-time within the coastal areas of East China Sea and South China Sea, which are connected by the Taiwan Strait. Results include vertical profiles from open ocean waters to moderate turbid waters and first lidar continuous observation of diel vertical distribution of thin layers at a fixed station. The root-mean-square relative differences between the HSRL and coincident in situ measurements are 5.6% and 9.1% for K_d and b_{bp}, respectively, corresponding to an improvement of 2.7–13.5 and 4.9–44.1 times, respectively, with respect to elastic backscatter lidar methods. Shipborne oceanic HSRLs with high performance are expected to be of paramount importance for the construction of 3D map of ocean ecosystem.

Introduction

Lidar techniques present distinctive abilities in ocean remote sensing, providing continuous vertical information of optical properties within the upper water column during both day- and night-time[1–3]. These techniques allow improving our understanding of marine ecosystems and biogeochemistry including the diel vertical migration of marine species[2], carbon cycles[4], annual cycles of polar phytoplankton abundance[1], phytoplankton layers[5,6] and Antarctic spring ice-edge blooms[7]. In addition to this, future perspectives for the lidar look bright because many scientific studies that could be effectively carried out, e.g., phytoplankton[8,9], carbon cycle[10], mesoscale eddies[11] and polar regions[12], lack continuous, diel, depth-resolved data. However, the ill-posed nature of elastic backscatter lidar retrievals and multiple scattering effects could limit the accuracy of existing lidar techniques, which harpers our investigation of marine ecosystems and biogeochemistry using lidar[3,13]. A major limitation of the elastic backscatter lidar is that it needs to infer two unknowns, attenuation and backscatter, from a single measurement, leading to an ill-posed problem[3]. Besides,

Correspondence: Dong Liu (liudongopt@zju.edu.cn)
[1]Ningbo Research Institute, State Key Laboratory of Modern Optical Instrumentation, College of Optical Science and Engineering, Zhejiang University, Hangzhou 310027, China
[2]Intelligent Optics & Photonics Research Center, Jiaxing Key Laboratory of Photonic Sensing & Intelligent Imaging, Jiaxing Research Institute, Zhejiang University, Jiaxing 314000, China
Full list of author information is available at the end of the article
These authors contributed equally: Yudi Zhou, Yang Chen, Hongkai Zhao

the laser propagation in seawater is accompanied by strong, nonnegligible multiple scattering effects, determining substantial difficulties in the retrieval, e.g., reliable products of the attenuation[14], size and shape[15,16] of ocean particles.

A variety of efforts have been made to solve the ill-posed problem of the lidar equation. Initially, various algorithms were proposed without changing the mechanism of elastic backscatter lidar, including slope method[17], Fernald method[18] and perturbation method[17] etc. Nevertheless, errors are still inevitable for each method has its own set of imperfect assumptions[3]. An important leap in retrieval accuracy has been achieved with the high-spectral-resolution lidar (HSRL) technique, which can independently measure backscattering and attenuation by separating the particulate and molecular backscatters in wavelength distribution. This technique has been used for decades in aerosols and clouds measurements based on Cabannes-Brillouin scattering from air molecules with broadening of ~3 GHz[19–22], and was recently developed for aircraft deployment in ocean detections[23,24] using the backscatter from water molecules shifted to both sides by ~7–8 GHz at 532 nm[25–27]. Despite high efficiency of airborne HSRL, its simultaneous measurements with in situ methods are difficult. Therefore, at scenes of multi-parameter observations, e.g., detections of temperature, salinity, current and phytoplankton when investigating interactions between physical ocean processes and ocean ecosystems, it would be beneficial to develop shipborne HSRL that can endure the harsh conditions on board and work with other shipborne equipment by providing in-flow continuous measurements over the depth.

Owing to the complexity of multiple scattering, several methods have been proposed to improve the retrieval accuracy based on the elaboration of effective theoretical models to analyze oceanic HSRL signals, mainly ranging from Monte Carlo (MC) simulations[28,29] to the simplified radiation transfer theory[30,31]. Typically, Gordon[29] suggested that signal attenuation is identified as the beam attenuation coefficient if the field of view (FOV) was small enough, while a large enough FOV corresponds to the diffuse attenuation coefficient. However, it is difficult to evaluate if the FOV is not large or small enough. Besides, it does not consider that the attenuation changes throughout the whole detection depth under multiple scattering. Walker and McLean[30] suggested that the attenuation coefficient is approximately equal to the absorption coefficient in shallow water and the diffuse attenuation coefficient in deep water, which avoided the FOV influence but still did not solve the problem of depth. Therefore, large errors could be introduced using these experiential conclusions. It would be extremely urgent to develop an algorithm to remove the multiple scattering effect on the attenuation considering the impacts of the FOV and depth.

We developed, to the best of our knowledge, the first shipborne oceanic HSRL and a multiple scattering correction (MSC) algorithm for rigorously addressing the above-mentioned challenges, the ill-posed nature of elastic backscatter lidar retrievals and multiple scattering. Underway continuous HSRL measurement are reported together with the first diel measurement at a fixed station, that were collected in the coastal areas of East China Sea (ECS) and South China Sea (SCS), which are connected by the Taiwan Strait. Measurements were carried out during both day- and night-time as a part of the 2020 Autumn Joint ECS&SCS cruise. In addition, comparisons between retrievals using HSRL, elastic backscatter lidar and in situ measurements were carried out.

Results

Shipborne oceanic HSRL

The operational principle of the shipborne oceanic HSRL is shown in Fig. 1. It transmits a laser pulse into the seawater and collects the backscattered echoes, known as the lidar signal, which contains depth-resolved seawater information, as shown in Fig. 1a. The attenuation and backscatter of laser radiations, and consequently the lidar signals, are sensitive to all optically active constituents, e.g., pure seawater, phytoplankton, colored-dissolved-organic matter (CDOM) and non-algal particles, etc. For example, a phytoplankton layer may generate a peak in the elastic backscatter signal, while CDOM only contributes to the attenuation. The HSRL system is divided into two major subsystems (Fig. 1b). The upper subsystem mainly consists of the laser head and the receiver, which can rotate from the horizontal position to nadir. Thus, a same lidar geometrical factor can be estimated after calibration in the horizontal position of atmosphere. The lower subsystem consists of computer, control boxes, a water-cooling system, a power supply and an air conditioner etc., which support the operation of the upper part. The system is integrally sealed to avoid the erosion from the sea salt and sea foam. Due to the strong background light, the laser light is not visible at day-time but it is clearly visible at night-time (up-left of Fig. 1b). The HSRL incident angle is ~60 degree during underway observation to avoid the ship spray and ~40 degree at the fixed station. The laser polarization direction is perpendicular to the light incident plane to ensure a small air-sea Fresnel reflectance at above the incidence angles[32].

The schematic diagram of the shipborne oceanic HSRL is illustrated in Fig. 1c and the key technical specifications of the HSRL are listed in Supplementary Table S1. An ultra-narrow (picometer) spectral discrimination is achieved through a series of transmitting and receiving techniques. Specifically, a diode-pumped, Q-switched,

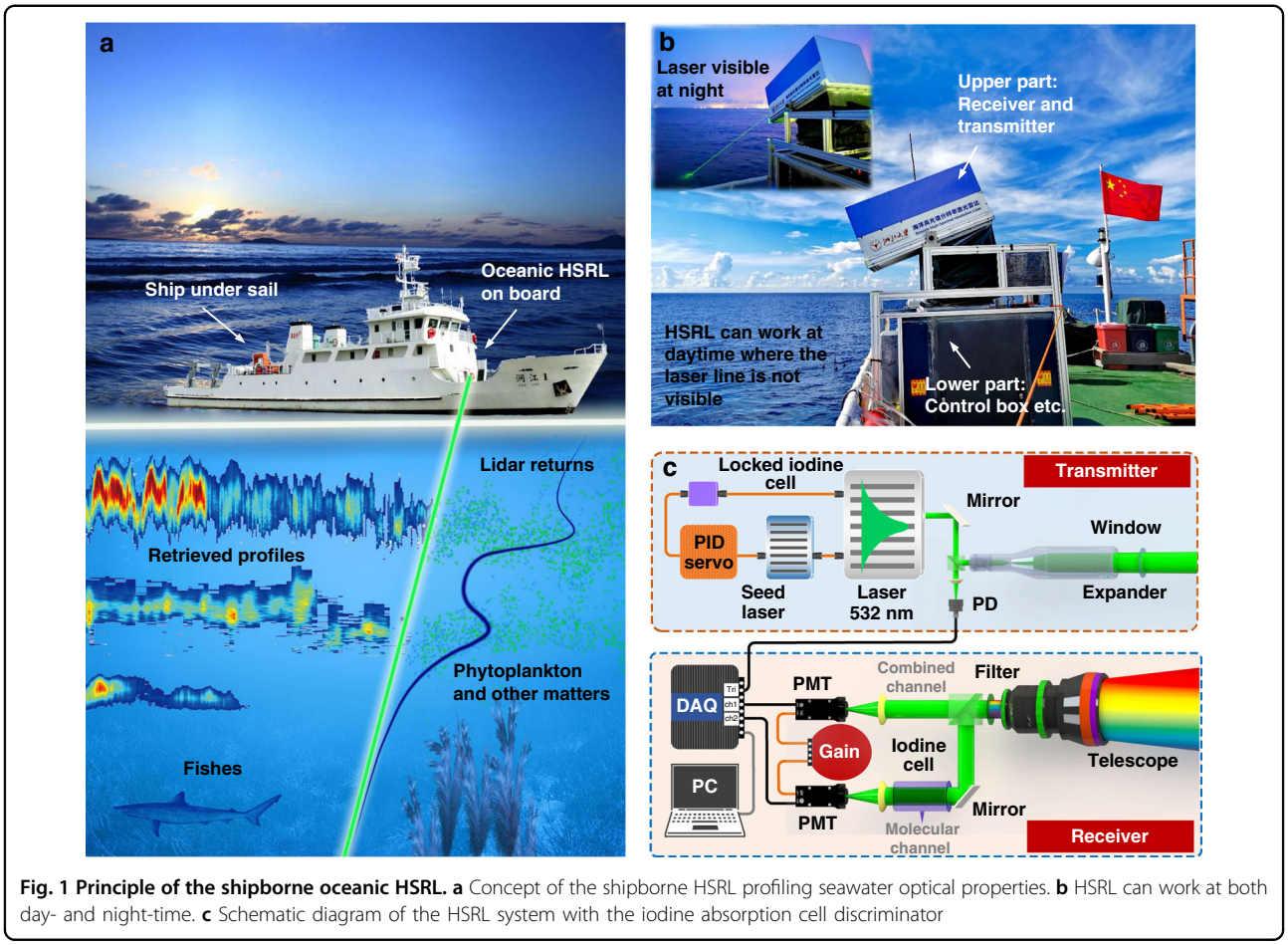

Fig. 1 Principle of the shipborne oceanic HSRL. a Concept of the shipborne HSRL profiling seawater optical properties. **b** HSRL can work at both day- and night-time. **c** Schematic diagram of the HSRL system with the iodine absorption cell discriminator

injection-seeded, frequency-doubled Nd-YAG laser at 532 nm is used, with a pulse energy of 10 mJ and a repetition frequency of 10 Hz. Through a proportional-integral-derivative (PID) servo loop, the frequency of the laser is locked to the absorption line of an iodine cell. The iodine stabilized laser is then transmitted into the water via an expander and a window. A photoelectric detector (PD) is used for triggering. When the laser hits the seawater, various optical interactions occur, including Rayleigh, Brillouin, Raman scattering from water molecules, particulate scattering and fluorescence from chlorophyll-a and CDOM, etc. The backscattered signal components are collected by a telescope with a diameter of 50.8 mm and an FOV of 200 mrad. The use of an interference filter centered at 532 nm with a bandwidth of 3 nm allows filtering out Raman scattering and fluorescence with shifted wavelengths, as well as most of background radiation. Then, transmitted signal components are split into two beams, conveyed to the combined and molecular channels, respectively. The combined channel collects all the components, while the molecular channel exploits the iodine cell ultra-narrow spectral discrimination (See methods for detail) to reject both the particulate and Rayleigh signals and transmits Brillouin signal. Photomultiplier tubes (PMT) and a high-speed data acquisition card with a sampling frequency of 400 MHz, equivalent to the distance resolution of 0.28 m in the water, are used to detect and sample the lidar signals.

Data processing

Flow chart of data processing from the raw data to retrieval products is illustrated in Fig. 2. The lidar signals of the combined and molecular channels are regarded as the raw data, as shown in up-left of Fig. 2. The scattering layer can be seen in the combined channel, while it disappears in the molecular channel as the particulate scattering is rejected by the discriminator. The preprocessing flowchart of the HSRL data are shown in up-right of Fig. 2. For a large FOV, the geometrical factor reaches unit after several meters in the atmosphere and will not influence signals in the water so it is not considered in the data preprocessing. The raw data are converted into standard format with time, location and system status. Then, the automatic removal of the sea foam (Supplementary Fig. S1) and identification of the sea level are carried out to eliminate the impact of waves and ship

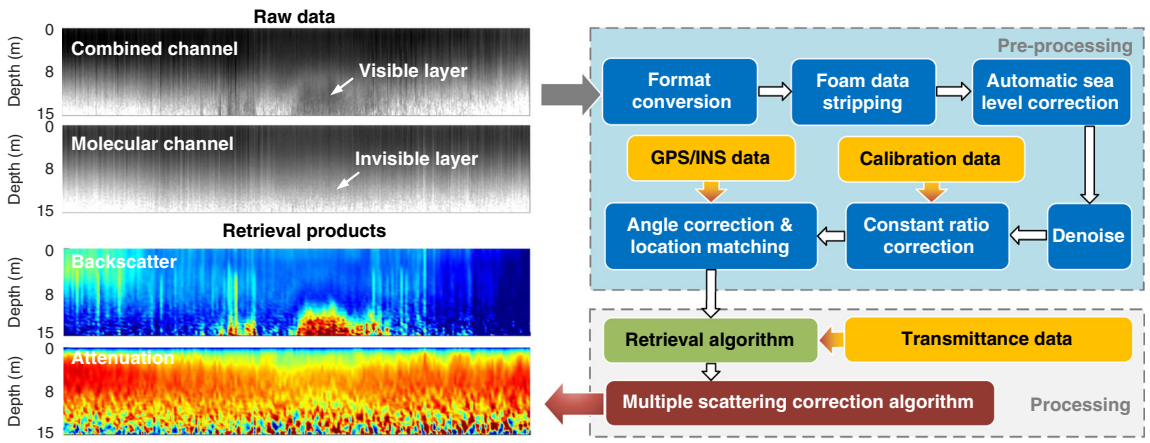

Fig. 2 Flow chart of HSRL data processing. Steps from raw data to retrieval products

fluctuation on the signal. For the denoising algorithm, the influence of the background and random noises on the signal is filtered out[28] (Supplementary Fig. S2). Then, the data of 0–3 m are removed to eliminate surface effects (e.g., bubbles) and the data with low SNR are removed, which are defined as the dynamic range of ~3–3.5 orders of magnitude considering the influence of the noise and tailing of system response. Furthermore, the detector gain ratio and channel efficiency ratio are calibrated for the constant ratio corrections. The interference of ship shaking and navigation location matching are considered using Global Position System (GPS) and Inertial Navigation System (INS) data. The pre-processing signals in combined and molecular channels are finally obtained as inputs of the retrieval algorithm. The processing flowchart of the HSRL data are shown in lower-right of Fig. 2. The retrieval algorithm outputs diffuse attenuation coefficient K_d, particulate backscatter coefficient b_{bp} and the lidar ratio R. Then, an MSC algorithm is proposed to revise K_d as well as R (see details in Methods). The retrieval products of K_d and b_{bp} are shown in lower-left of Fig. 2

Underway measurements

During the Autumn 2020 Joint ECS and SCS cruise with the *R/V Runjiang No.1*, continuous underway HSRL measurements (~800 km) were carried out from Sep. 6 to Sep. 8 with the ship track and study region shown in Fig. 3a. The digital topographic data is from the ETOPO1 Global Relief Model (Methods). Discrete in situ optical properties, temperature and salinity were obtained at stations S_1-S_5 (Methods). The spatial variability of the water column bio-optical properties, namely the chlorophyll-a concentration (Chl), the suspended sediment concentration (SSC) and the colored dissolved organic matter absorption at 440 nm (a_{CDOM}) is illustrated using the L2B products of the China ocean color satellite HY-1C, as shown in Fig. 3b–d, respectively (Methods). Then, the water depth versus Chl, SSC and a_{CDOM} along the ship track (red lines) of Fig. 3a–d are illustrated in Fig. 3e.

The profiles of b_{bp}, K_d and R by HSRL are plotted in Fig. 3f–h. The red lines in Fig. 3f–h are 3 optical depths that are defined as the product of the depth and the attenuation coefficient, which is used for the assessment of lidar detection depth[3]. The black regions in Fig. 3f–h are not considered due to the low signal-to-noise ratio (SNR). In the region close to the Zhejiang and the Fujian Provinces, namely the north section from Start (start of measurement session) to S_1, values of Chl, SSC and a_{CDOM} (Fig. 3e) are high[33,34] since most of the sediments transported by rivers are trapped in estuaries or deposited on adjacent continental shelves of ECS[35]. b_{bp} and K_d values of ~0.1 m^{-1} and ~0.5 m^{-1} lead to a detection depth generally smaller than 10 m as the SNR decreases rapidly. For the Taiwan Strait area (the south section from Start to S_1), Chl and a_{CDOM} values (Fig. 3e) are similar to those in the north section, while SSC values change dramatically. b_{bp} and K_d values are lower and the detection depth can reach 10–15 m. In the south part of Taiwan Strait (from S_1 to S_2), SSC values (Fig. 3e) of the Taiwan Shoal are much higher than values in the surrounding areas that presumably include open ocean water[33]. Similarly, values of b_{bp} and K_d are ~0.0045 m^{-1} and ~0.1 m^{-1}, respectively, in the Taiwan Shoal, but decrease to ~0.001 m^{-1} and ~0.08 m^{-1}, respectively, in the surrounding areas. For the northern SCS area, which is close to Guangdong Province (from S_2 to S_4), values of Chl, SSC and a_{CDOM} (Fig. 3e) are much lower and SSC is almost close to the minimum detection limit because generally SCS is much clearer than ECS[36]. Similarly, values of b_{bp} and K_d decrease to ~0.001 m^{-1} and ~0.07 m^{-1}, respectively. From S_4 to End (end of measurement session), gradually approaching the

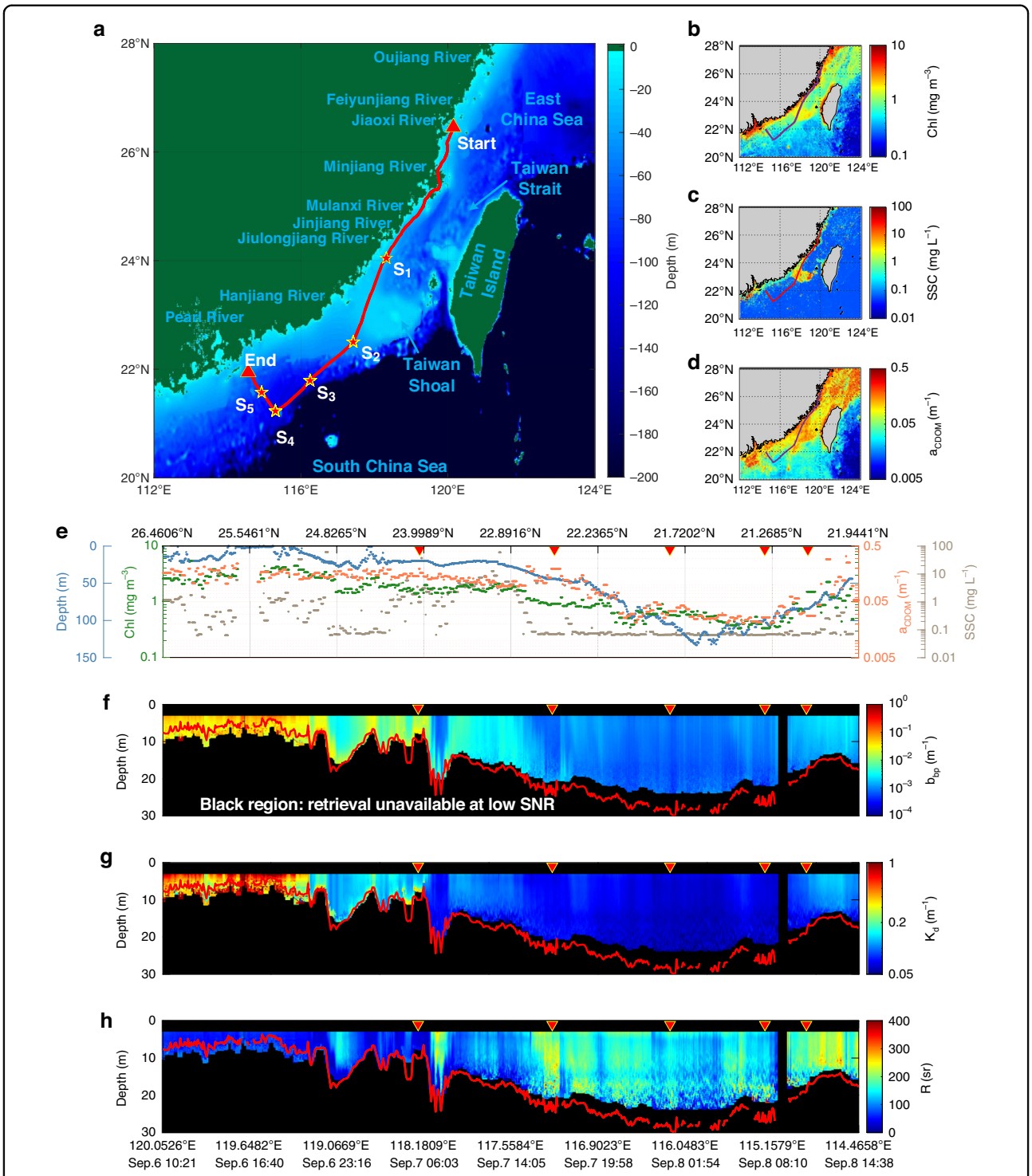

Fig. 3 Continuous underway HSRL measurements (~800 km). Plots of **a** water depth from ETOPO1, **b** Chl, **c** SSC, **d** a_{CDOM} from HY-1C (Methods) with the ship track represented with the red lines. Discrete in situ measurements were obtained at stations S_1-S_5 (Methods). **e** Values along the ship track in Fig. 3a–d. Profiles of **f** b_{bp}, **g** K_d, **h** R retrieved by HSRL with 3 optical depths in red lines

shoreside, values of Chl and a_{CDOM} gradually increase, while SSC values remain low. Values of b_{bp} and K_d are ~0.002 m^{-1} and ~0.11 m^{-1}, respectively. Generally, trends in b_{bp} and K_d from HSRL measurements seem to agree with those observed for the Chl, SSC and a_{CDOM} products derived from HY-1C.

The lidar attenuation to backscatter ratio R from HSRL is an important index for the characterization of water composition (Fig. 3h). Churnside et al.[37] reported lidar ratio values close to 100 for values of Chl lower than 3 mg m^{-3} for Case 1 water, where phytoplankton abundance is high compared to nonbiogenic particles and absorption by Chl and related pigments represents a major contribution in the total absorption coefficient[38]. Obviously, the experimental water belongs to Case 2 water that are "everything else except Case 1"[38] since Chl is not the only dominant factor as shown in Fig. 3e. Chl, SSC and CDOM contribute to the light absorption while only Chl and SSC contribute to light backscattering. Generally, R values in Fig. 3h are lower in the transect ranging from Start to S_2 than from S_2 to End because high SSC concentrations determine the high backscatter values found in the former transect, while SSC values decrease to nearly zero and Chl and CDOM dominate in the latter transect. It is to be specified that almost constant SSC values of ~1 mg L^{-1} from Start to S_2 produce different values of R, e.g., ~50 sr from Start to S_1 but ~150 sr from S_1 to S_2 perhaps due to the monthly average of SSC. Interestingly, between S_1 and S_2, values of R of ~80 sr in the Taiwan Shoal are much lower than its surrounding areas (~220 sr) centered at (118.05°E, 23.82°N) and S_2 (117.33°E, 22.50°N). For S_2, high a_{CDOM}, low Chl and very low SSC values could explain high R values. Around (118.05°E, 23.82°N), values of SSC highly fluctuate, but Chl and a_{CDOM} values are similar to those found in the Taiwan Shoal so it is possible that the sailing route crossed the front between the ECS Coastal Current and Taiwan Warm Current preventing the high SSC water from being transported to the shelf[33]. In addition, R values from S_5 to End are larger than those found in the Taiwan Shoal between S_2 and S_3 while their K_d are similar, perhaps due to the SSC variability from ~3 mg L^{-1} to 0.1 mg L^{-1}. R values can also be different at different vertical levels. For example, R values observed for the scattering layer moving from a depth of 5 m to a depth of 10 m around (24.8265° N, 119.0669° E) are much smaller than those found outside such layer, as shown in Supplementary Fig. S3. A possible motivation for this variability is that the layer is close to the water bottom and is characterized by high SSC, which in turn can reduce R values. Overall, for most of the data collected during the cruise, the water column composition, especially the values of SSC, is highly correlated to R values.

Diel measurement

During the Autumn 2020 Joint ECS&SCS cruise, a diel continuous measurement was carried out on Sep. 14, 2020 at a fixed station S_6, which is close to the Shimei Bay of the SCS, as shown in Fig. 4a–d. The water depth is 48 m and the Chl, SSC and a_{CDOM} values derived from HY-1C at this station were 0.54 mg m^{-3}, 0.07 mg L^{-1} and 0.04 m^{-1}, respectively (Methods). The sunrise and sunset time were 06:25 and 18:42 (UTC + 08:00), respectively. Note that the UTC + 08:00 is adopted in the following text unless otherwise stated. Discrete in situ measurement of the optical properties, temperature and salinity were collected at different time (T_1–T_5) (Methods).

The b_{bp}, K_d and R values retrieved from HSRL data are shown in Fig. 4e, f, respectively, where the first lidar diel continuous observation of scattering layers for a given fixed station is presented. Since b_{bp} is sensitive to the suspended particulate matter, it is not surprising to find scattering layers named as L1-1, L1-2, L2-1, L2-2, L3 and L4 in Fig. 4e throughout the whole day. L1-1 is about 2 m thick and located at the depth of ~5 m at 03:00. However, the depth gradually increases to ~10 m at 09:00. L1-2 layer, that is most probably the continuation of L1-1, shows a depth decrease from ~10 m at 9:00 to ~5 m at 14:00. L2-1 and its possible continuation L2-2 fluctuated around a depth of 15 m from 03:00 to 14:00. Apparently, L1-2 and L2-2 gradually merged into L3 after 14:00 for which the depth gradually decreased up to ~5 m from 15:00 to 00:00. L4 was intermittent from 10:00 to 24:00 as the depth then was beyond the detection range of the HSRL. From 18:00 to 22:00, its depth became shallower and the background noise became lower so that it could be detected continuously. In addition, it is interesting that the wild fluctuations of depths of all layers in a short time are simultaneous. The appearance of layers is probably caused by the internal waves. As shown in Supplementary Fig. S4, Sentinel-1A Synthetic Aperture Radar (SAR) quick-look image of internal waves in the Shimei Bay is taken at the same day as the lidar observation (10:46:16 UTC on Sep. 14, 2020). Although internal wave edges are not very clear, it presents a similar pattern as demonstrated by Churnside and Ostrovsky[39]. Notably, R values observed within the layers are smaller than those of the surrounding areas (Fig. 4g), which can be also observed around T_5 (see details in Supplementary Fig. S5), thus allowing to infer the change of water column properties.

In Fig. 4e and Supplementary Fig. S6a, the increase of b_{bp} appeared in the time intervals 09:00–15:00 and 21:00–00:00. The seawater temperature and salinity, measured every 2 h, were subtracted by their mean values at each depth to obtain their anomalies, as shown in Supplementary Fig. S6b, c. It is interesting to find a decreased temperature and increased salinity between 09:00–15:00 and 21:00–00:00, which might be caused by upwelling that brought the deep cold water with high salinity and nutrient to the surface. Considering sunlight contribution, it is possible that an increase of both nutrient and light led to the phytoplankton rising between 09:00–15:00, while the increase of b_{bp} between

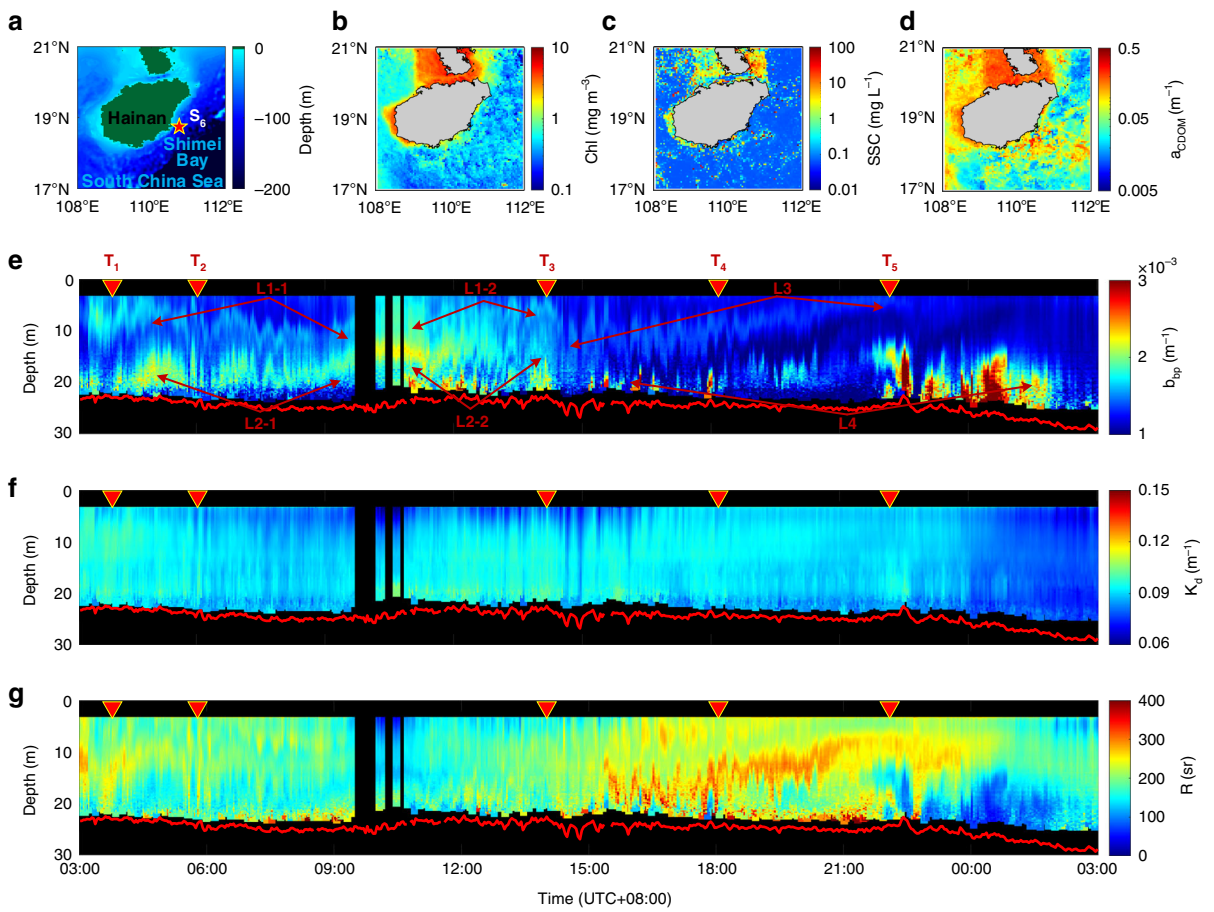

Fig. 4 A diel continuous measurement for a fixed station. Plots of **a** water depth from ETOPO1, **b** Chl, **c** SSC, **d** a_{CDOM} from HY-1C (Methods) with the ship track in red lines. Profiles of **e** b_{bp}, **f** K_d, **g** R retrieved by HSRL with 3 optical depths in red lines. Discrete in situ data were collected at different time T_1-T_5 (Methods)

21:00–00:00 might be attributed to the upwelling of phytoplankton and sediment close to the bottom.

Consistency check

As shown in Fig. 5, K_d and b_{bp} values from HSRL are validated using in situ measurements (green) and compared with several methods applied to the elastic backscatter lidar signals from the HSRL (Methods). The orange represents outputs of HSRL retrieval algorithm and blue refers to K_d of HSRL-MSC algorithm in Fig. 2. The methods applied to the elastic backscatter lidar signals include the Fernald method[18] based on different lidar ratios of 100 sr (gray) and 200 sr (black) and the perturbation method[5] (purple). The data at S_1-S_5 in Fig. 3 and at T_1-T_5 in Fig. 4 are adopted.

As shown in Fig. 5a, it reveals that K_d values from the Fernald method ($R = 100$ sr adopted for Case I water[37]) deviate furthest from the in situ results due to the inappropriate R value[18], as shown in Supplementary Fig. S7. After changing R to 200 sr, K_d of Fernald method decreased and approached to the in situ results. Although R is still smaller than the in situ results, as shown in Supplementary Fig. S7, the consistency seems good due to the algorithm convergence. The perturbation method only outputs a constant K_d value along the water column but is close to in situ data probably because of the small influence of inhomogeneous backscatter on the attenuation. As for HSRL, the vertical distribution of K_d can be obtained independently without a priori assumptions of the lidar ratio. However, the derived K_d value is slightly larger than the in situ measurements because of the strong influence of multiple scattering. Then, K_d agrees better with the in situ values after adopting MSC algorithm.

Furthermore, the higher accuracy of HSRL over elastic backscatter lidar can be well supported by the b_{bp} results, as shown in Fig. 5b. Generally, the degrees of deviation from the in situ values follow the scheme "Fernald (100) > perturbation > Fernald (200) > HSRL" although it is not similar for S_1 perhaps due to small in situ lidar ratio.

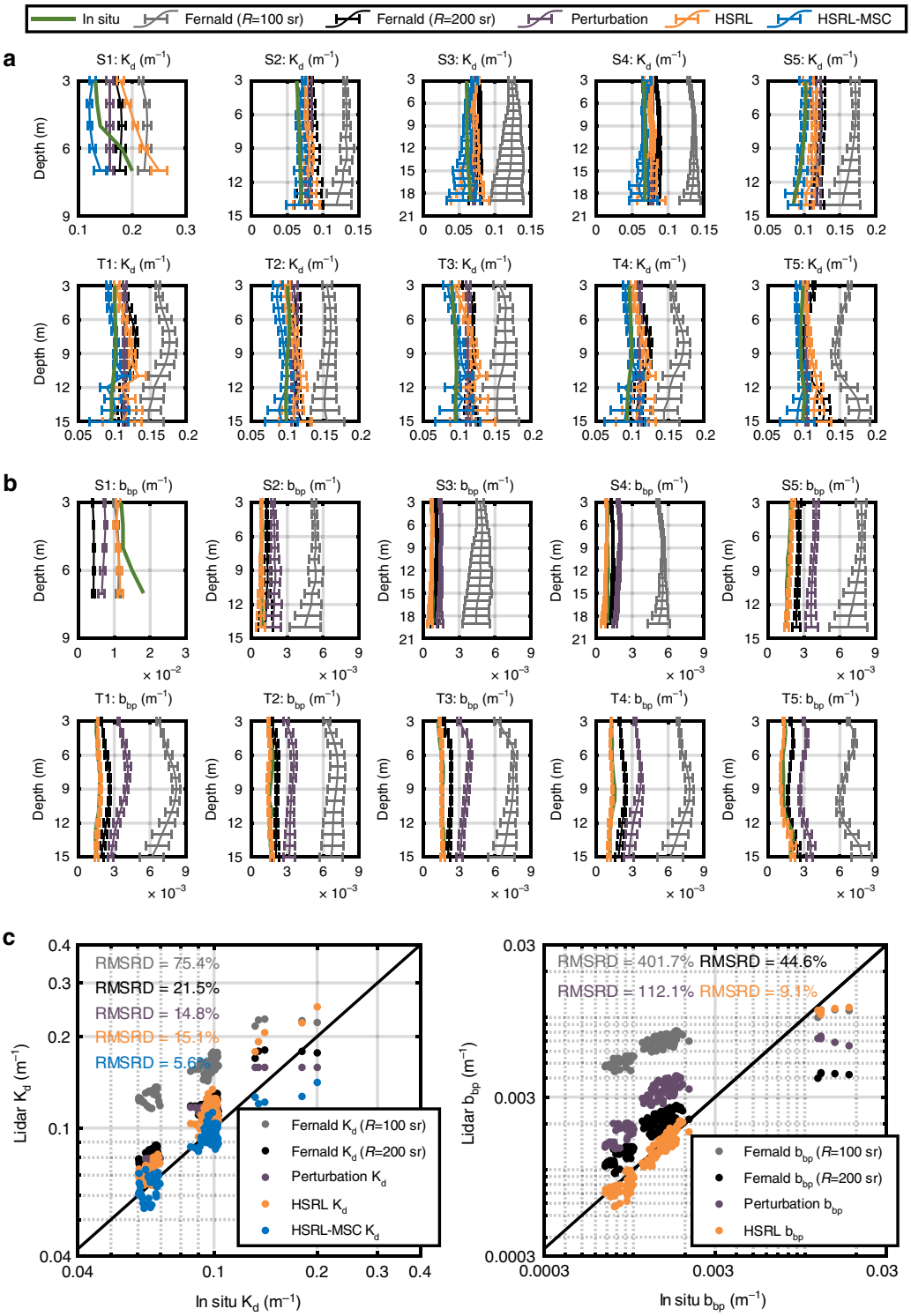

Fig. 5 The consistency check of HSRL retrievals. a Comparisons of K_d. **b** Comparisons of b_{bp}. The orange represents outputs of HSRL retrieval algorithm and blue refers to K_d of HSRL retrieval and MSC algorithm in Fig. 2. Fernald method based on lidar ratios of 100 sr (gray) and 200 sr (black) and perturbation method (purple) are used for the elastic backscatter lidar. All lidar results are validated by in situ measurements (green) in **c** statistical analysis of K_d and b_{bp}

In Supplementary Fig. S7, perturbation method obtains a similar R of 100 with Fernald (100) because they are both based on the bio-optical method of Case 1 water. However, the effects of unreasonable R on the accuracy of Fernald method seem larger than that of perturbation method. If R values are changed to 200 sr, the accuracy of Fernald method is improved.

Then, the results are analyzed in Fig. 5c. The root mean square relative difference (RMSRD) is utilized here for reflecting the HSRL performance realistically, that is,

$$\mathrm{RMSRD}(\%) = 100\sqrt{\frac{\sum_{i=1}^{N}\left(x_i/\widetilde{x}_i - 1\right)^2}{N}} \quad (1)$$

where N is the total number of sampling points, x_i is the lidar-measured value and $\widetilde{x}_i$ is the in situ measured value. As shown in Fig. 5c, it shows that the RMSRD of K_d and b_{bp} ranges from 15.1–75.4% and 44.6–401.7% for the methods of elastic backscatter lidar, respectively. The RMSRD of K_d between the HSRL and in situ measurements is 15.1%, and that of b_{bp} is 9.1%. Furthermore, the MSC algorithm reduces the RMSRD of K_d by a factor of 2.7, typically from 15.1% to 5.6%. Overall, the HSRL-MSC results remarkably improve the accuracy by factors of 2.7–13.5 and 4.9–44.1 for K_d and b_{bp}, respectively, relatively to the elastic backscatter lidar retrievals. The strong correlations ($r^2 = 0.86$ for $\log_{10}(K_d)$ and $r^2 = 0.94$ for $\log_{10}(b_{bp})$) were also observed between in situ and HSRL-MSC measurements. In general, HSRL and HSRL-MSC demonstrate more accurate estimations of K_d and b_{bp} than elastic backscatter lidar methods.

Discussion

In this paper, we developed, to the best of our knowledge, the first shipborne oceanic HSRL for which none a priori assumptions of the lidar ratio are required. It is achieved by using an ultra-narrow spectral discrimination in the picometer order through a series of techniques including single longitudinal mode laser, iodine absorption cell with accurate controlling of temperature and frequency locking part. An MSC algorithm for rigorously addressing the multiple scattering is proposed to further promote the retrieval accuracy. The HSRL-MSC RMSRDs are 5.6% for K_d and 9.1% for b_{bp} during the 2020 Autumn Joint ECS&SCS cruise, which remarkably improves the accuracy by factors of 2.7–13.5 and 4.9–44.1 for K_d and b_{bp}, respectively, relatively to the elastic backscatter lidar methods. The accuracy are a little better than those of 17.2% for K_d and 27.1% for b_{bp} from the NASA airborne HSRL system[23], which might be related to several factors, although the retrieval accuracy varies amongst study areas. There are often spatial and temporal gaps between the lidar and in situ measurements, which may cause different measured water[23,40]. Fortunately, the gaps can be almost ignored in this paper since the lidar and in situ method both worked on the ship. Furthermore, the utilization of MCS algorithm could be another reason that promotes the accuracy of K_d. Note that the algorithm can also be adopted at other lidar systems after changing the system parameters.

Although airborne and spaceborne lidar can cover regional or global ocean[1,2,4–6,16,24], shipborne lidar can illuminate our understanding of the underlying biological/physical/chemical processes in ocean by combining lidar and other shipborne measurements[8,24,41–43]. For example, when any anomaly is detected, the in situ measurements can be easily deployed to validate and investigate the HSRL results (Supplementary Fig. S6). Moreover, shipborne lidar has potential to penetrate deeper than airborne or space-borne lidars because of less atmosphere influence and closer distance to water surface. Also, the shipborne oceanic HSRL can provide continuous measurements of the depth-resolved bio-optical properties, which is more difficult to get from in situ measurements on the ship, e.g., WETLabs acs used in this paper. Considering the huge advantages of accuracy, simultaneous measurements with in situ methods and spatial-temporal sampling, the shipborne HSRL proposed in this study could be of primary importance for the following issues: 1) to improve the understanding of ocean biological, physical and biogeochemical processes by resolving the vertical structure within the upper water column; and 2) to validate the existing and future spaceborne lidar missions dedicated to the ocean.

Thin layers that are often related to ocean biological and physical process attract wide interests[8,43]. However, it is difficult to find layers based on in situ measurements due to the complex sampling steps and limited sampling stations. HSRL technique increases the likelihood to detect layers through continuous observation, allowing direct quantification of thin layer characteristics and dynamics. Also, the shipborne HSRL could be conveniently operated together with other sampling technologies to recognize the layer compositions and understand the associated environmental conditions[44]. Except thin layers, the shipborne HSRL is able to characterize the vertical heterogeneity of other matters in the ocean, which are expected to contribute to many scientific studies, such as carbon cycle[4] and eddies[11].

The lidar ratio R of HSRL can be a proxy of the Chl:b_{bp} ratio because Chl is directly related to K_d in Case 1 waters. Such a ratio has been proved useful for tracking changes in phytoplankton community composition[24,45]. Low values of Chl:b_{bp} ratio are associated with pico- and nano-phytoplankton while high values are associated with diatom dominated phytoplankton communities[45]. Schulien et al.[24] showed that changes in airborne HSRL measurements coincided with a shift in phytoplankton community

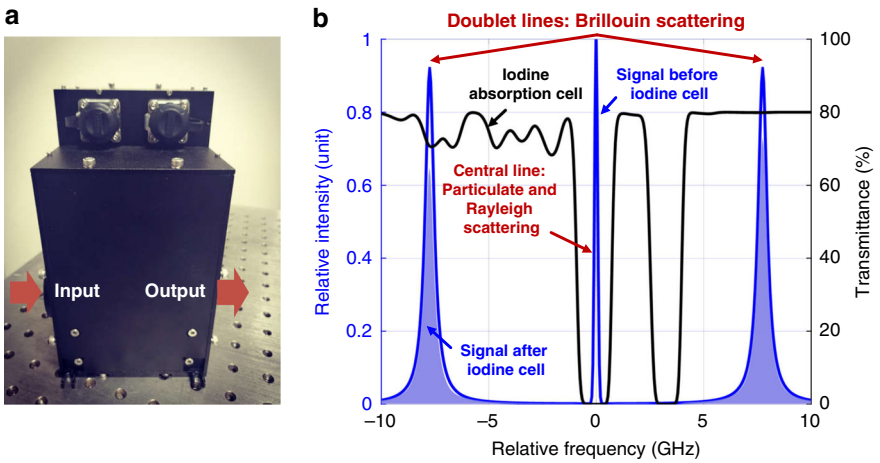

Fig. 6 The ultra-narrow discrimination of the iodine cell. a The picture of the packed iodine absorption cell integrated with the temperature controller. The light enters the device from the left and leaves from the right. **b** Illustration of the spectral discrimination, where the iodine cell (black line) filters the signal (blue line) by rejecting the particulate and molecular Rayleigh signals and transmitting molecular Brillouin signal (blue shadow)

composition across an anticyclonic eddy in the North Atlantic. In addition, the Chl:b_{bp} ratio can reflect the photoacclimation state of the phytoplankton cell[9].

The powerful performance of shipborne HSRL is of great interest for the validation of the current and future spaceborne lidar missions for ocean observation. Recently, spaceborne lidars such as Cloud-Aerosol Lidar and Orthogonal Polarization (CALIOP) greatly promoted our knowledge about phytoplankton in polar regions[1] and daily vertical migrations of ocean animals[2]. Besides, the additional information on the size and the shape of ocean particles potentially can be provided from CALIOP[16]. Another spaceborne lidar designed for ice, cloud and land elevation measurements, Advanced Topographic Laser Altimeter System (ATLAS), was able to provide information on Antarctic spring ice-edge blooms[7]. Future spaceborne lidar missions dedicated to ocean will further improve our understanding of ocean ecosystem functioning[3]. However, there are only a few studies that validated such an approach[4,40]. Therefore, it will be useful and convenient for shipborne HSRL to significantly contribute to supporting the validation of the spaceborne lidar.

Despite development of shipborne oceanic HSRL, the potential of lidar has not been fully realized. In the future, it is expected to develop multi-wavelength HSRL based on the existing HSRL at 532 nm[3,6]. The fielded-widen Michelson interferometric spectral filter or Fabry-Pérot interferometric filter can be utilized as optional ultra-narrow discriminators in wavelengths outside 532 nm[26] but the contradiction between the more wavelengths and more difficult manufacturing technique of laser will limit the lidar wavelength. The multi-wavelength technique can provide more information about CDOM, Chl and bring us to the bottom of euphotic layer in the open ocean, which can strengthen our understanding of the maximum Chl layer. In addition, with the development of oceanic polarized lidar simulation technique, it is possible to interpret the depth-resolved depolarized information from multiple scattering[46]. The information of depolarization is directly related to the microphysical information of particles, like shapes, which could improve our understanding of phytoplankton species community[15,16].

Materials and methods

Ultra-narrow discrimination

The iodine cell is exploited in the molecular channel for ultra-narrow spectral discrimination, as shown in Fig. 1c. The packed iodine absorption cell is integrated with the temperature controller (Fig. 6a). The light enters the device from the left and leaves from the right. Then the cell could reject both the particulate and Rayleigh signals centered at the laser wavelength and transmits Brillouin signal shifting to the both sides of the center with a frequency shift of about 7–8 GHz (Fig. 6b). There are several iodine absorption lines that can be exploited in the HSRL technique and here we select the 1104 line (Supplementary Fig. S8), with the central wavelength at ~532.2928 nm. The laser emission, the particulate backscatter signals and 1104 iodine line have coincident wavelengths.

HSRL retrieval algorithm

The retrieval algorithm of HSRL has already been proposed[25,26] but can be simplified when the molecular Brillouin transmittance T_B is large while the particulate

and Rayleigh transmittance T_p and T_R is tiny, that is,

$$b_{bp}(z) = 2\pi\chi\beta_p^{\pi} \tag{2}$$

where $\beta_p^{\pi} = \beta_B^{\pi}[T_B B_C(z)/B_M(z-1]$, B_C and B_M are the signals of combined and molecular channels, z is the water depth, β_B^{π} and β_p^{π} is the Brillouin and particulate 180° volume scattering function[38], χ is the conversion factor that connects β_p^{π} and b_{bp} with a selected value of 1.0[47]. T_B and T_p are calibrated and calculated by scanning iodine absorption lines. The lidar attenuation coefficient can be written as

$$k_{lidar}(z) = -\frac{1}{2}\frac{d}{dz/\cos\theta_r}\ln\left[B_M(z)\cdot\left(\frac{nH}{\cos\theta_i}+\frac{z}{\cos\theta_r}\right)^2\right] \tag{3}$$

where n is the refractive index of the seawater, H is the HSRL working height above the water surface, θ_i and θ_r are the angles of incidence and refraction in the atmosphere and seawater, respectively. k_{lidar} is generally regarded as the diffuse attenuation coefficient K_d in a large FOV[29].

Then, the lidar ratio R is defined as

$$R(z) = \frac{K_d(z) - K_{d,w}}{\beta_p^{\pi}} \tag{4}$$

where $K_{d,w}$ is the diffuse attenuation coefficient of the pure seawater.

Multiple scattering correction algorithm

There are several simulating and experimental results[14,23,30] not totally support the approximation that k_{lidar} is regarded as K_d in a large FOV[29]. In fact, k_{lidar} changes with depth considering multiple scattering even in a homogeneous water[14,30]. Here, considering the relationship between inherent optical properties (IOPs) and k_{lidar}[48], we developed an MSC algorithm, which transfers k_{lidar} to K_d by correcting the effects of multiple scattering. The MSC algorithm is established as follows:

Step 1: The analytical model based on the quasi-single small-angle approximation[49] is built for the simulation of molecular signals with a flat molecular backward phase function.

Step 2: Molecular signals are simulated using the analytical model under several IOPs conditions listed in Supplementary Table S2. Signals and k_{lidar} derived from Eq. (3) are plotted in Supplementary Figs. S9 and S10. Note that the angles of inclination are different in underway measurement and at the fixed station, which is considered in the simulation of Supplementary Figs. S9 and S10, respectively.

Step 3: It is interesting to find that the simulated k_{lidar} in Supplementary Figs. S9 and S10 have similar patterns, which is small near the surface but increase with the depth. Moreover, k_{lidar} seems to be proportional to the absorption. Therefore, a model for this pattern is proposed as

$$k_{lidar} = m_1 \times \exp(-m_2 \times z) + m_3 + a \tag{5}$$

where a is the absorption coefficient, b_b is the backscattering coefficient, z is the depth, m_1, m_2 and m_3 are model parameters. As shown in Supplementary Figs. S9 and S10, it demonstrates good agreements between the simulated and modeled k_{lidar} with the values of m_1, m_2 and m_3 shown in Supplementary Tables S3 and S4.

Step 4: The m_1, m_2 and m_3 are then found to be described by functions based on the backscattering coefficient with high R^2, as shown in Supplementary Figs. S11 and S12. It means that k_{lidar} can be described by a and b_b according to Eq. (5).

Step 5: Then, it is necessary to validate the reliability of Eq. (5). The IOPs in Supplementary Table S5 are used in simulation of molecular signals and k_{lidar} for validation. As shown in Supplementary Fig. S13, the modeled and simulated k_{lidar} show good consistency with R^2 of ~0.98 and RMSRD of ~4%, where the definition of RMSRD is similar to Eq. (1).

Step 6: Combining Eq. (5) and the empirical relationship between K_d and IOPs proposed by Lee et al.[50], the MSC algorithm can be written as:

$$K_d = k_{lidar} - m_1 \times \exp(-m_2 \times z) - m_3 + 4.18 \times b_b \times \left[1 - 0.52 \times e^{-10.8(k_{lidar} - m_1 \times \exp(-m_2 \times z) - m_3)}\right] \tag{6}$$

Then, the MSC-corrected K_d can be obtained by substituting HSRL-measured k_{lidar} from Eq. (2) and b_b from Eq. (3) into Eq. (6). Then the lidar ratio R is updated with the MSC-corrected K_d using Eq. (4).

Elastic backscatter lidar methods

Perturbation method, that follows the description of Churnside and Marchbanks[5], and Fernald method[18] (Supplementary Section S1) are used for retrievals of elastic backscatter lidar using the combined channel of HSRL as signals.

In situ measurement

The in situ absorption and backscatter coefficients at 532 nm were collected and calculated by WETLabs acs and HOBILabs HS6P, from which the in situ K_d was derived according to the algorithm by Lee et al.[50]. The in situ temperature and salinity data were provided by a

Sea-Bird Electronics, Inc. conductivity-temperature-depth device. See Supplementary Section S2 for detailed illustration.

Topographic and remote sensing data

The digital topographic data from the ETOPO1 Global Relief Model published by the National Geophysical Data Center are available at http://www.ngdc.noaa.gov/mgg/global/global.html. The Chl, SSC and a_{CDOM} from L2B products of the China ocean color satellite HY-1C in Sep. 2020 are available at https://osdds.nsoas.org.cn, where a_{CDOM} are corrected by the field data[34]. The Sentinel-1A SAR data from European Space Agency are available at https://asf.alaska.edu/.

Acknowledgements

This study was supported by Excellent Young Scientist Program of Zhejiang Provincial Natural Science Foundation of China (LR19D050001); National Key Research and Development Program of China (2016YFC1400900); Fundamental Research Funds for the Central Universities (International team); Scientific Research Foundation for Talent Introduction (20201203Z0175, 20201203Z0177) of Zhejiang University Ningbo Campus; Project of Hangzhou Institute of Environmental Protection Science; State Key Laboratory of Modern Optical Instrumentation Innovation Program; Photonics and Electronics for Innovations of Belarusian State Research Program; Zhejiang University Global Partnership Fund. The authors want to thank insightful discussions from Dr. Mike Behrenfeld at Oregon State University, USA, Dr. Heather Bouman at Oxford University, UK and Dr. Zhongping Lee at the University of Massachusetts, USA about lidar data and ocean science. We thank National Satellite Ocean Application Service, China and National Geophysical Data Center, USA for the ocean color and bathymetry data. We thank the captain and all the crews of R/V *Runjiang No.1* for the assistance and support in the field experiment and scientists at Second Institute of Oceanography, China for collecting in situ data. We also thank the support from International Space Science Institute for supporting international team of satellite oceanic lidar.

Author details

[1]Ningbo Research Institute, State Key Laboratory of Modern Optical Instrumentation, College of Optical Science and Engineering, Zhejiang University, Hangzhou 310027, China. [2]Intelligent Optics & Photonics Research Center, Jiaxing Key Laboratory of Photonic Sensing & Intelligent Imaging, Jiaxing Research Institute, Zhejiang University, Jiaxing 314000, China. [3]Univ. Littoral Côte d'Opale, CNRS, Univ. Lille, IRD, UMR 8187 - LOG - Laboratoire d'Océanologie et de Géosciences, F-62930 Wimereux, France. [4]Institute of Marine Sciences (ISMAR), Italian National Research Council (CNR), Rome - Tor Vergata 00133, Italy. [5]Sorbonne Université, CNRS, LATMOS, 96 Boulevard de l'Observatoire, 06304 Nice Cedex, France. [6]Scuola di Ingegneria, Università della Basilicata, Viale Ateneo Lucano 10, I-85100 Potenza, Italy. [7]Cooperative Institute for Research in Environmental Sciences, University of Colorado Boulder and NOAA Chemical Sciences Laboratory, 325 Broadway, Boulder, CO 80305, USA. [8]Institute of Physics, National Academy of Sciences of Belarus, Pr. Nezavisimosti 68-2, Minsk 220072, Belarus. [9]Key Laboratory for Ecological Environment in Coastal Areas (State Oceanic Administration), National Marine Environmental Monitoring Center, Dalian 116023, China. [10]CAS Key Laboratory of Tropical Marine Bio-Resources and Ecology, South China Sea Institute of Oceanology, Chinese Academy of Sciences, Guangzhou 510301, China. [11]School of Atmospheric Sciences and Guangdong Province Key Laboratory for Climate Change and Natural Disaster Studies, Sun Yat-sen University, Zhuhai 519000, China. [12]Faculty of Technology and Environment, Prince of Songkla University, Phuket 83120, Thailand. [13]Second Institute of Oceanography, Ministry of Natural Resources, Hangzhou 310012, China. [14]Ocean College, Zhejiang University, Zhoushan 316021, China. [15]Donghai Laboratory, Zhoushan 316021, China

Author contributions

D.L. and Y.Z. conceived the idea; D.L., Y.C., N.W., P.X., B.W., F.C., C.Y. and C.L. designed and built the HSRL instrument; Y.T.C., Q.L. and K.Z. established the MSC algorithm; H.K.Z., Y.Z., A.M., and X.W. processed HSRL data; Y.T., T.C. and C.F.L. processed the passive data; Y.C. and P.C. prepared the in situ data; C.J., D.D., M.C., P.G. and J.C. contributed to data analysis; H.D.Z., Z.Y., D.Q. and S.P. provided the explanation of ocean science; Y.Z., D.L. and H.K.Z. wrote the manuscript with contributions from all co-authors. D.L. supervised the research.

Competing interests

The authors declare no competing interests.

Supplementary information The online version contains supplementary material available at https://doi.org/10.1038/s41377-022-00951-0.

Received: 16 February 2022 Revised: 18 July 2022 Accepted: 7 August 2022
Published online: 02 September 2022

References

1. Behrenfeld, M. J. et al. Annual boom-bust cycles of polar phytoplankton biomass revealed by space-based lidar. *Nat. Geosci.* **10**, 118–122 (2017).
2. Behrenfeld, M. J. et al. Global satellite-observed daily vertical migrations of ocean animals. *Nature* **576**, 257–261 (2019).
3. Hostetler, C. A. et al. Spaceborne lidar in the study of marine systems. *Annu. Rev. Mar. Sci.* **10**, 121–147 (2018).
4. Behrenfeld, M. J. et al. Space-based lidar measurements of global ocean carbon stocks. *Geophys. Res. Lett.* **40**, 4355–4360 (2013).
5. Churnside, J. H. & Marchbanks, R. D. Subsurface plankton layers in the Arctic Ocean. *Geophys. Res. Lett.* **42**, 4896–4902 (2015).
6. Chen, P. et al. Vertical distribution of subsurface phytoplankton layer in South China Sea using airborne lidar. *Remote Sens. Environ.* **263**, 112567 (2021).
7. Lu, X. M. et al. Antarctic spring ice-edge blooms observed from space by ICESat-2. *Remote Sens. Environ.* **245**, 111827 (2020).
8. Sengupta, A., Carrara, F. & Stocker, R. Phytoplankton can actively diversify their migration strategy in response to turbulent cues. *Nature* **543**, 555–558 (2017).
9. Behrenfeld, M. J. et al. Revaluating ocean warming impacts on global phytoplankton. *Nat. Clim. Change* **6**, 323–330 (2016).
10. Behrenfeld, M. J. et al. Climate-driven trends in contemporary ocean productivity. *Nature* **444**, 752–755 (2006).
11. Mahadevan, A. et al. Eddy-driven stratification initiates North Atlantic spring phytoplankton blooms. *Science* **337**, 54–58 (2012).
12. Arrigo, K. R. et al. Massive phytoplankton blooms under Arctic Sea ice. *Science* **336**, 1408–1408 (2012).
13. Jamet, C. et al. Going beyond standard ocean color observations: lidar and polarimetry. *Front. Mar. Sci.* **6**, 251 (2019).
14. Liu, D. et al. Phase function effects on the retrieval of oceanic high-spectral-resolution lidar. *Opt. Express* **27**, A654–A668 (2019).
15. Collister, B. L. et al. Polarized lidar and ocean particles: insights from a mesoscale coccolithophore bloom. *Appl. Opt.* **59**, 4650–4662 (2020).
16. Dionisi, D. et al. Seasonal distributions of ocean particulate optical properties from spaceborne lidar measurements in Mediterranean and Black sea. *Remote Sens. Environ.* **247**, 111889 (2020).
17. Churnside, J. H. et al. Ocean backscatter profiling using high-spectral-resolution lidar and a perturbation retrieval. *Remote Sens.* **10**, 2003 (2018).
18. Fernald, F. G. Analysis of atmospheric lidar observations: some comments. *Appl. Opt.* **23**, 652–653 (1984).
19. Shipley, S. T. et al. High spectral resolution lidar to measure optical scattering properties of atmospheric aerosols. 1: theory and instrumentation. *Appl. Opt.* **22**, 3716–3724 (1983).
20. Hair, J. W. et al. Airborne High Spectral Resolution Lidar for profiling aerosol optical properties. *Appl. Opt.* **47**, 6734–6752 (2008).
21. Wang, N. C. et al. Dual-field-of-view high-spectral-resolution lidar: simultaneous profiling of aerosol and water cloud to study aerosol-cloud interaction. *Proc. Natl Acad. Sci. USA* **119**, e2110756119 (2022).
22. Ke, J. et al. Development of China's first space-borne aerosol-cloud high-spectral-resolution lidar: retrieval algorithm and airborne demonstration. *PhotoniX* **3**, 17 (2022).

23. Schulien, J. A. et al. Vertically-resolved phytoplankton carbon and net primary production from a high spectral resolution lidar. *Opt. Express* **25**, 13577–13587 (2017).
24. Schulien, J. A. et al. Shifts in phytoplankton community structure across an anticyclonic eddy revealed from high spectral resolution lidar scattering measurements. *Front. Mar. Sci.* **7**, 493 (2020).
25. Hair, J. et al. Combined atmospheric and ocean profiling from an airborne high spectral resolution lidar. *EPJ Web Conf.* **119**, 22001 (2016).
26. Zhou, Y. D. et al. Retrieving the seawater volume scattering function at the 180° scattering angle with a high-spectral-resolution lidar. *Opt. Express* **25**, 11813–11826 (2017).
27. Zhou, Y. D. et al. Multiple scattering effects on the return spectrum of oceanic high-spectral-resolution lidar. *Opt. Express* **27**, 30204–30216 (2019).
28. Liu, D. et al. Lidar remote sensing of seawater optical properties: experiment and Monte Carlo simulation. *IEEE Trans. Geosci. Remote Sens.* **57**, 9489–9498 (2019).
29. Gordon, H. R. Interpretation of airborne oceanic lidar: effects of multiple scattering. *Appl. Opt.* **21**, 2996–3001 (1982).
30. Walker, R. E. & Mclean, J. W. Lidar equations for turbid media with pulse stretching. *Appl. Opt.* **38**, 2384–2397 (1999).
31. Malinka, A. V. & Zege, E. P. Analytical modeling of Raman lidar return, including multiple scattering. *Appl. Opt.* **42**, 1075–1081 (2003).
32. Born, M. & Wolf, E. *Principles of optics: electromagnetic theory of propagation, interference and diffraction of light* 7th edn. (Cambridge: Cambridge University Press, 2013).
33. Bian, C. W. et al. Distributions of suspended sediment concentration in the Yellow Sea and the East China Sea based on field surveys during the four seasons of 2011. *J. Mar. Syst.* **121-122**, 24–35 (2013).
34. Zhou, F. X. et al. Absorption properties of chromophoric dissolved organic matter (CDOM) in the East China Sea and the waters off eastern Taiwan. *Continental Shelf Res.* **159**, 12–23 (2018).
35. Liu, J. P. et al. Flux and fate of Yangtze river sediment delivered to the East China Sea. *Geomorphology* **85**, 208–224 (2007).
36. Xing, X. G. et al. Temporal and vertical variations of particulate and dissolved optical properties in the South China Sea. *J. Geophys. Res. Oceans* **124**, 3779–3795 (2019).
37. Churnside, J. H., Sullivan, J. M. & Twardowski, M. S. Lidar extinction-to-backscatter ratio of the ocean. *Opt. Express* **22**, 18698–18706 (2014).
38. Mobley, C. D. *Light and water: radiative transfer in natural waters* (San Diego: Academic Press, 1994).
39. Churnside, J. H. & Ostrovsky, L. A. Lidar observation of a strongly nonlinear internal wave train in the Gulf of Alaska. *Int. J. Remote Sens.* **26**, 167–177 (2005).
40. Bisson, K. M. et al. Particulate backscattering in the global ocean: a comparison of independent assessments. *Geophys. Res. Lett.* **48**, e2020GL090909 (2021).
41. Sun, H. Y. et al. Detection of surface defects and subsurface defects of polished optics with multisensor image fusion. *PhotoniX* **3**, 6 (2022).
42. Collister, B. L. et al. Remote sensing of optical characteristics and particle distributions of the upper ocean using shipboard lidar. *Remote Sens. Environ.* **215**, 85–96 (2018).
43. Durham, W. M., Kessler, J. O. & Stocker, R. Disruption of vertical motility by shear triggers formation of thin phytoplankton layers. *Science* **323**, 1067–1070 (2009).
44. Durham, W. M. & Stocker, R. Thin phytoplankton layers: characteristics, mechanisms, and consequences. *Annu. Rev. Mar. Sci.* **4**, 177–207 (2012).
45. Cetinić, I. et al. A simple optical index shows spatial and temporal heterogeneity in phytoplankton community composition during the 2008 North Atlantic Bloom Experiment. *Biogeosciences* **12**, 2179–2194 (2015).
46. Liu, Q. et al. A semianalytic Monte Carlo radiative transfer model for polarized oceanic lidar: Experiment-based comparisons and multiple scattering effects analyses. *J. Quant. Spectrosc. Radiat. Transf.* **237**, 106638 (2019).
47. Churnside, J. H. Review of profiling oceanographic lidar. *Optical Eng.* **53**, 051405 (2014).
48. Liu, Q. et al. Relationship between the effective attenuation coefficient of spaceborne lidar signal and the IOPs of seawater. *Opt. Express* **26**, 30278–30291 (2018).
49. Zhou, Y. D. et al. Validation of the analytical model of oceanic lidar returns: comparisons with Monte Carlo simulations and experimental results. *Remote Sens.* **11**, 1870 (2019).
50. Lee, Z. P., Du, K. P. & Arnone, R. A model for the diffuse attenuation coefficient of downwelling irradiance. *J. Geophys. Res. Oceans* **110**, C02016 (2005).